International Journal of Latest Research in Engineering and Technology (IJLRET)
ISSN: 2454-5031
www.ijlret.com || Volume 04 - Issue 08 || August 2018 || PP. 34-51

Geometry Effects on Failure Mechanisms of Hybrid Metal-Composite Bolted Joints

Calin-Dumitru COMAN[1]
[1]*Department of Structures and Materials, INCAS Bucharest, Romania*

Abstract: This paper presents the effects of geometry variation on the damage initiation and growth in the CFRP (Carbon Fiber Reinforced Polymer) composite laminated plate of the single-lap, single-bolt, hybrid metal-composite joints. A detailed 3D finite element model (FEM) incorporating geometric, material and friction-based contact full nonlinearities is developed to numerically investigate the geometry effects on the progressive damage analysis (PDA) of the orthotropic material. The PDA material model integrates the lamina nonlinear shear response, Hashin-tape failure criteria and strain-based continuum degradation rules, which were developed using the UMAT user subroutine in Nastran commercial software. In order to validate the geometry variation effects on the failure modes of the protruded head bolted joints, experiments were conducted using the SHM (Structural Health Monitoring) nondestructive testing technique. The results showed that the plate geometry is an important parameter in the design process of an adequate bolted joint and its effects on damage initiation and failure modes were quite accurately predicted by the PDA material model, which proved to be computationally efficient and can predict failure propagation and damage mechanisms in hybrid metal-composite bolted joints.

Keywords: Progressive Failure, Nonlinear Shear Deformation, Hybrid Joints, SHM

1. INTRODUCTION

The aerospace industry became the most common application field for fiber-reinforced polymer matrix composites (PMCs) due to their lightweight properties [1]. These structural components are often assembled in conjunction with metal parts using mechanically fastened joints resulting in hybrid metal-composite joints which generate some challenging issues for mechanical engineers. Poorly designed hybrid joints are not only a source of failure, but could lead to a reduction of the durability and reliability of the whole structure. Up to nowadays, the researchers studied the failure analysis of composite bolted joints using a method that combines continuum damage mechanics (CDM) [2] with finite element analysis (FEA). In the CDM models, the local damage onset appears at a low values of applied load and damage accumulation is developed with increasing load according to damage propagation laws, which makes the method accurate and able to predict various failure modes. The major disadvantage of the CDM models is the huge amount of test data required for model calibrations. The progressive damage analysis (PDA) of composite materials, which is based on the stress-strain failure criterion, showed that the material orthotropic properties reduction due to damage initiation is essential for the stress field analysis [3-7]. Many PDA models [8-11] incorporated lamina shear nonlinearity, Hashin-type failure criterion and constant elastic properties degradation laws for orthotropic materials, which make the method quite easy to implement and computationally efficient. Because these properties degradation models used constant factors for elastic properties reduction due to damage growth, the models weren't be able to predict the bearing final failure.

Models containing continuous degradation rules started to appear in the literature [12], [13] as to improve the numeric algorithm converge and to obtain a smoother load-displacement curve. One major lack of these models is that they focused only on few types of failure modes and were not considering the various joint failure modes. The composite progressive damage behavior is a complex nonlinear phenomena and in conjunction with geometric and contact nonlinearities can lead to loss of convergence in the finite element method analysis, mostly in implicit numerical algorithms which imply that many effortsare paid for obtaining a valid solution towards the ultimate global structure failure [14].The difficulties arising from composite materials usage on structural failure problems, are that these materials have anisotropic mechanical properties, brittle and low inter-laminar strength [15].

Awadhani et *al*. [16] presented a numerical and experimental study for the influence of a geometry parameter (edge distance to bolt diameter ratio, *e/d*) onto the stiffness, strength and failure modes of the hybrid metal-GFRP (Glass Fibers Reinforced Plastic) single-lap, single-bolt joints with steel bolts. The conclusion of the study was that the *e/d* ratio varied the failure modes from cleavage to bearing mode. It was also observed that the geometric parameter has increased the joint tensile strength; load at yield increased also.

In this study it is presented and developed a progressive damage analysis using an adequate material

model for composite plate that can predict the effects of geometry parameters (width to bolt diameter -*w/d*- and edge distance bolt diameter -*e/d*- ratios)variation on structural behavior and failure modes of the hybrid metal-composite bolted joints. This model takes into account all the nonlinearities phenomena involved in load transfer as geometric nonlinearity which imply large deformations, friction based full nonlinear contact and material nonlinearities due to shear deformations of the lamina. Hashin-type failure criteria and strain-based continuous degradation lawswere implemented using a user subroutinedeveloped in FORTRAN programming languageand commercial Nastran SOL 400 solver. A series of experiments were conducted in order to validate the FE model and PDA results involving the influence of temperature on the failure modes of the hybrid-metal composite joints. The experimental and numerical results fit quite accurate for the influence of geometry parameters on the stiffness and failure load of hybrid metal-composite bolted joints.

2. PROBLEM DESCRIPTION

2.1 Joint geometry description

Single-lap joints (SLJ) with single hexagonal head bolt were manufactured using both metal and composite materials for the adherents. The geometry design was chosen in accordance with ASTM D5961 standard [17] to induce bearing failure. The in plane dimensions of the each plate of the joint are presented in Table 1 and Fig.1. The plate's thicknesses are different, 4 mm for the metal plate and 3 mm for the laminated plate. Hexagonal head stainless steel bolts with nominal diameter of 5 mm were used. The applied torque level for bolts is 0.5 N m, applied in dry conditions. The composite plate was made from carbon-epoxy pre-pregs with 32% fiber volume fraction. The stacking sequence of the laminated plate is represented by [0/90/0/90/0/90] using 0.33 mm thickness unidirectional laminae, with the elastic properties presented in Table 2. The metal plate was manufactured from aluminum alloy AA 7075T6 [18] and the bolts, nuts and washers were made from stainless steel A2-70 [18] with the elastic properties presented in Table 2, as well. A lot of five SLJ's for each case presented in Table 1 were prepared for the thermal effects study on the failure mechanisms in the laminated plate. The experimental models are presented in Fig.2.

Table 1. Experiment set-up

Geometry case	Nb. of specimens	Length (mm)	Width (mm)	Edge distance *e*(mm)	Torque (Nm)	Temperature (^{o}C)
1	5	150	34	10	0.5	+50
2		150	42	15		
3		150	50	20		

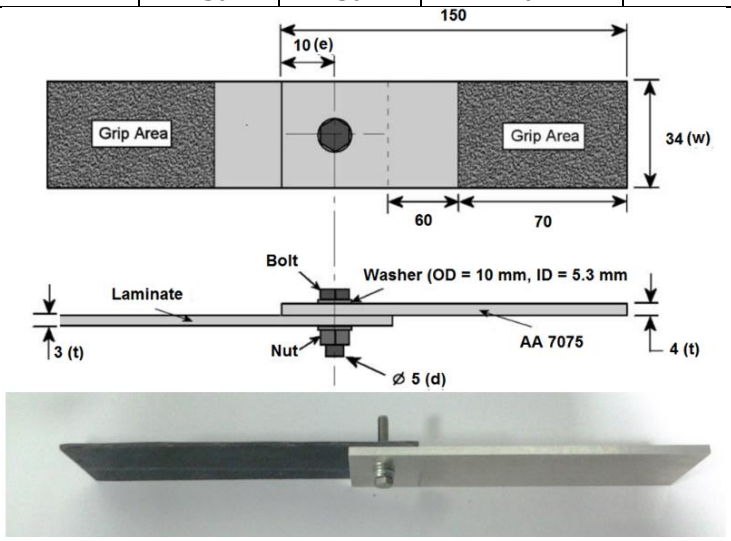

Fig.1. Joint geometry, geometry case 1

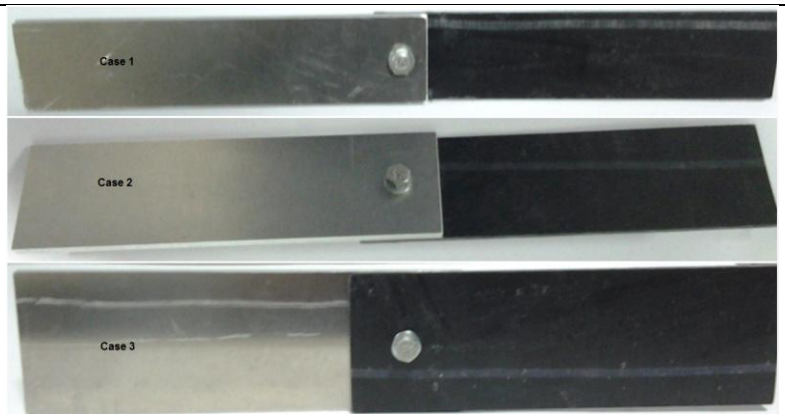

Fig. 2. Experimental models, geometry cases

Table 2. Mechanical properties of the materials

Property	CFRP Lamina	AA 7075T6 Ref. [18]	A2-70 Ref. [18]
Longitudinal modulus E_{11} (MPa)	34433	71016	206000
Transversal modulus E_{22} (MPa)	3610		
Through-thickness modulus, E_{33} (MPa)	3610		
Shear modulusG_{12} (MPa)	2421	26890	75842
Shear modulusG_{23} (MPa)	2421		
Shear modulusG_{13} (MPa)	1561		
Poisson coefficient $\square_{12}$	0.36	0.33	0.36
Poisson coefficient $\square_{23}$	0.45		
Poisson coefficient $\square_{13}$	0.35		
Longitudinal tensile strength $\sigma_{11,\,max}^{T}$,(MPa)	253		
Longitudinal compression strength $\sigma_{11,\,max}^{C}$, (MPa)	230		
Transversal compression strength $\sigma_{22,\,max}^{C}$, (MPa)	74		
In plane shear strengthτ_{12}^{max}, (MPa)	25		
Out plane shear strengthτ_{23}^{max}, (MPa)	37		
Out plane shear strengthτ_{13}^{max}, (MPa)	37		

Note: (1, 2, 3) are the lamina on axis coordinate system.

The unidirectional lamina properties presented in Table 2were obtained using ASTM [19]-[21] standards on the unidirectional laminated coupons. The bearing tests were conducted in accordance with ASTM standard [17]: the specimens were gripped into a 30kN Instron universal testing machine, the torque level was applied to the bolt and then the quasi-static displacement with 0.3 mm/min was applied until ultimate failure, as it is shown in Fig. 3.

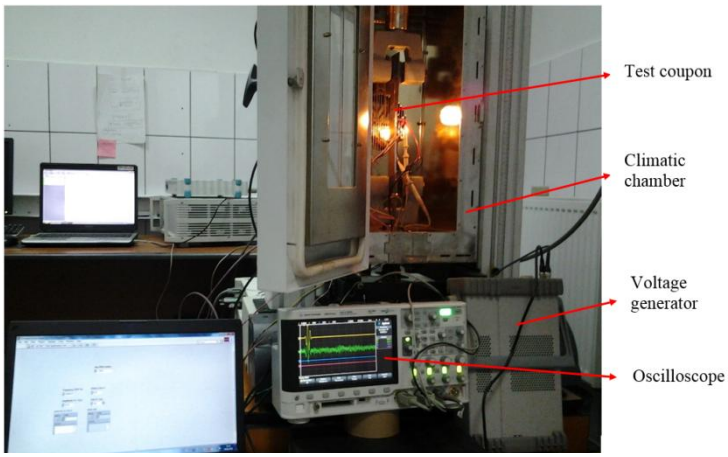

Fig.3. Experimental workbench

2.2 Numerical analysis

A tridimensional (3D) finite element model, using linear eight nodes brick elements, was developed in the commercial software MSC. Patran for the joint geometry shown in Fig. 5. Each separate part was meshed: the metal and composite plates, the washer and a combined bolt-nut part. The plates were meshed with high radial mesh density around the hole, where high strain gradients exists. In order to avoid rigid body motions, light springs were attached to the components not fully constrained, such as the bolt, washer and laminate plate. For simulating the bolt preload due to the torque level, a 330 Naxial forcewas applied in the bolt shank using Bolt Preload Module in Patran. This is done by sectioning the bolt shank in the shear plane location which separates the shank in two parts and creates coincident nodes at the interface cutting plane. These coincident nodes are then connected by an over-closure MPC (Multi Points Constrain) and loaded with axial preload.

Regarding the clamping of the joint in the test machine, the boundary conditions imposed on the model are presented in Fig.4 and represent fixing all the translations only on top and bottom surfaces of the leftmost end of the metal plate and blocking only the translations in y and z directions, imposing a prescribed displacement in x direction at the rightmost end of the composite plate.

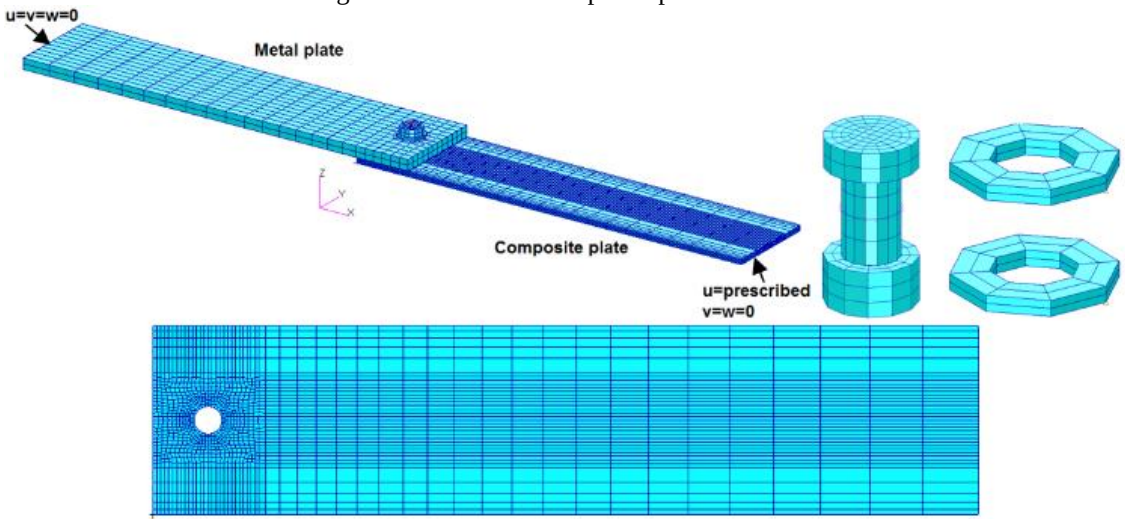

Fig. 4. 3D finite element model and boundary conditions

The laminated plate is modelled with continuum solid-shell special elements available in MSC Nastran 2012. These special solid elements have bending properties like shells and one integrating point per element is considered. The finite element model has six elements per laminate thickness, with one solid-shell element per each ply, thus, stress in each ply can be determined and the correct bending-twisting coupling is obtained. All metallic parts are modelled with continuum solid elements with large strain property assumed. In the 3D model, the contact between the bolt and the surface of the hole is achieved by the direct method of the constraints explained in the following. The method requires the definition of the bodies that can come into contact. The contact bodies may be the whole physical bodies (laminated plates, bolt, washer), but it has been shown [22] that it is more efficient to consider sets of elements of these physical bodies in contact, as shown in Fig. 5, because the number of checks for contact between bodies at each iteration of the solution is reduced.

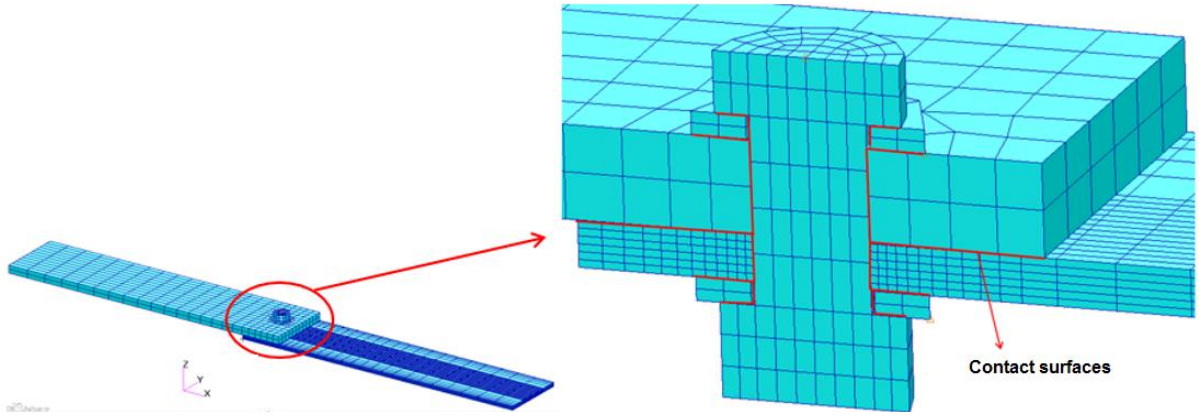

Fig. 5. Contact elements in 3D model

Another step in defining nonlinear contact phenomena is the choice between the analytical and discreet contact, which will be briefly described below. When a node on a solid reaches the contact segment on the other solid, the node is constraint on this segment along the normal to this segment. In the case of discrete contact for normal determination, the linear representation with the finite elements of the contact surface is used which leads to the calculation of the normal direction of each element. If the surface is not planar, when the node is touching the contact segment on the surface of the other solid, being in the tolerated contact area, it is shifted and constrained on the contact segment, making it possible for the moving process and constraint.The surface having a curve, the node is blocking between two different normal elements due to the discontinuity of the normal elements. This impediment has an adverse effect on the quality of the results as observed by McCarthy et *al*. [22] in their work on single bolt compositejoints. In the case of analytical contact, a smooth Coons surface is constructed through the nodes of the solid contact segment and then this analytical surface is used to calculate the continuous normal at the contact surface between the two bodies, thus it is solving the problem of blockingnode due to the discontinuity of the normal between the bodies. This method leads to a better representation of the geometry of the joint, especially its deformation and the accuracy of the numerical results is far superior to the technique of discrete contact, [22].

3. GEOMETRY EFFECTS ON JOINT FAILURE

3.1 Model validation

In this section, the results from the tests are compared with the results of the three-dimensional finite element model described in the previous chapter. Strains at selected points on the surface of the laminated plate are used to check the accuracy of the finite element model. The joints were strain gauged and loaded in tensile to a level that prevents any damage of the composite plate (1.2kN) and a 0.5 Nm torque level. Fig. 6 presents the locations of the strain gauges with 3 mm length; all gauges are aligned with the loading direction and located on the top surface of the laminate plate, except the gauge number 2 which is located in the shear plane on the bottom surface.The numerical and experimental results for strains are showed in Table 3 and Fig. 7.

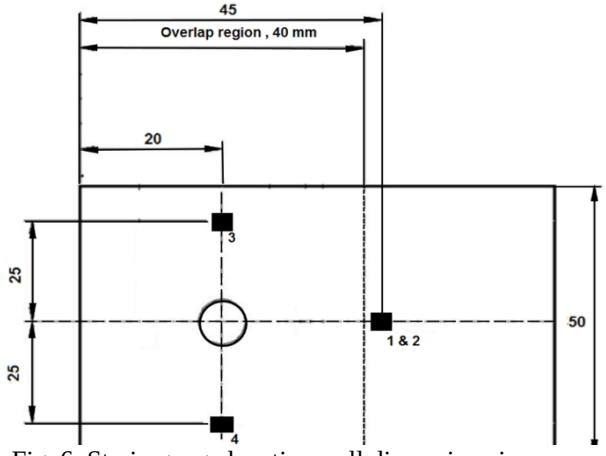

Fig. 6. Strain gauge locations, all dimensions in mm

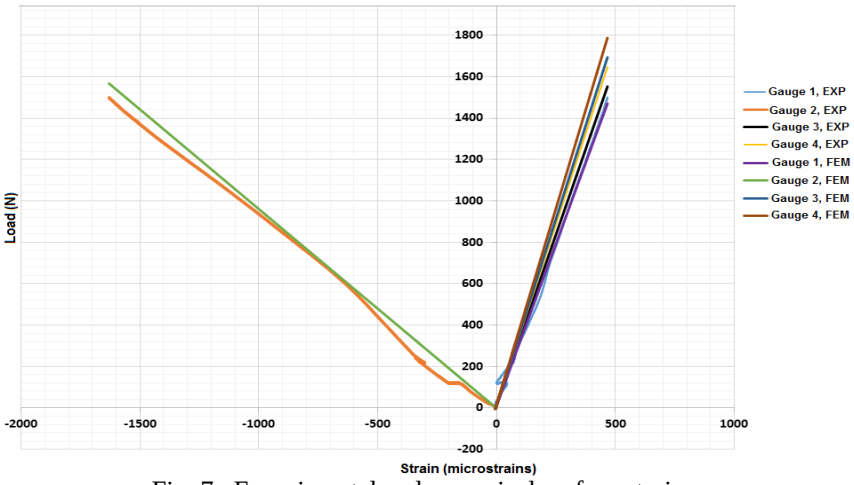

Fig. 7. Experimental and numerical surface strains

Table 3. Experimental and numerical strain gauge results, 1.2 kN applied load

Gauge number	Experimental strain (μm/m)	Numerical strain (μm/m)
1	376	380
2	-1300	-1252
3	357	329
4	339	315

From the Table 3 it is clearly seen that strain gauges 1 and 2 are indicating a joint bending despite the fact that the loading is a tensile applied load. The readings for gauges 3 and 4 are quite different, that indicating a twisting effect of the joint along the longitudinal axis which is the loading axis. As a conclusion, from the Table 3, it can be considered that the model predicted the linear behavior of the joint satisfactory and can be used in the following geometric parametric study for the failure mode of the hybrid metal-composite joint.

3.2 Joint stiffness

The effects of geometric parameters (*w/d, e/d*) on the axial stiffness of the hybrid metal-composite joints are presented in this paragraph. From the experimental load-displacement curves shown in Fig. 8, it can be seen that the linear-elastic range is developed from 0.3 kN up to 1.2 kN applied load for all the geometry cases, so the joint stiffness is determine for the linear approximation for this range.The joint load was obtained directly from testing machine and the displacement was measured with optical extensometers.

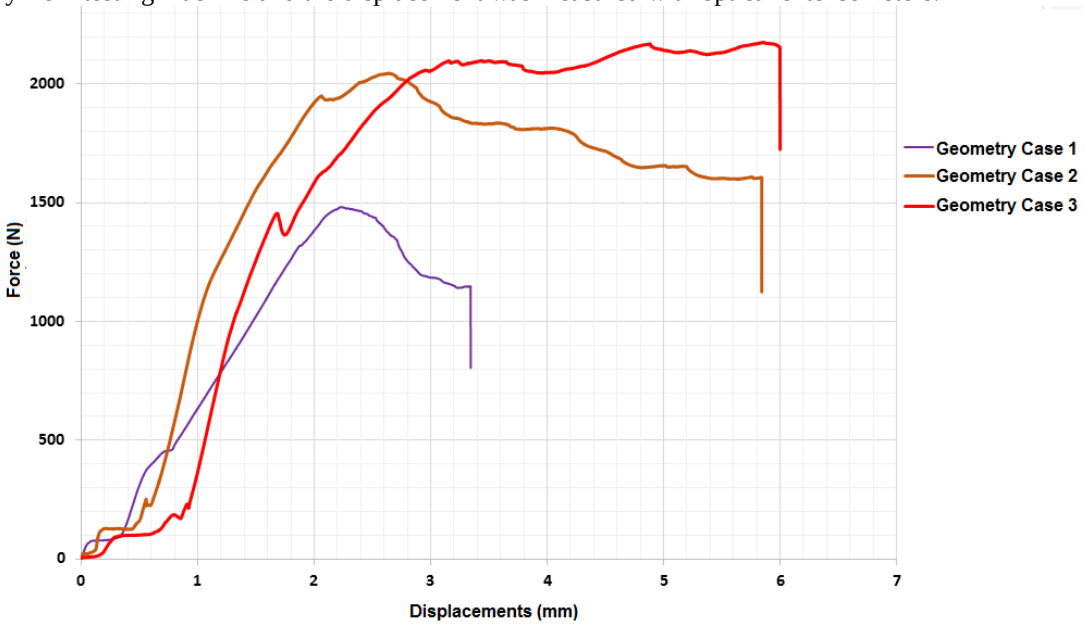

Fig.8. Load-displacements experimental curves

The first nonlinear segments on the experimental curves from Fig. 8 are explained by the friction between the plates. For low level of the applied load, the forces are transmitted through friction and the plates don't move relatively to each other, so the shank of the bolt don't bear the hole surface due to the initial clearance fit in the joint. The joint under investigation has a close tolerance clearance equal to 48 μm according to f7H10 standard fit tolerances.

As long as $F > 2\mu P$, where F is the applied joint load, $\mu=0.235$ is the frictional coefficient between aluminum AA 7075 and CFRP plates, as Schon [23] measured experimentally and P = 330 N is the plates clamping force due to preload, the friction is overcome and the bolt shank bears the hole surface. From now on, the joint is elastically deformed, the axial stiffness is fully developed and can be determined. The experimental and numerical axial stiffness, calculated as the slope of the approximately linear portions of the load-displacement curves, are presented in Table 4. From Table 4 and Fig.8, it can be observed that the geometric parameters increase the stiffness of the hybrid metal-composite joints in both experiment and simulation results.

Table 4. Joint axial stiffness

Geometry case	Torque [Nm]	Temperature [^{o}C]	Stiffness [N/mm]	
			EXP.	FEM
1 (*w/d*=6.8, *e/d*=2)	0.5	+50	784.313	744.879
2 (*w/d*=8.4, *e/d*=3)			2191.489	1936.251
3 (*w/d*=10, *e/d*=4)			2224.291	2093.834

3.3 SHM method description

A common and useful method for structure health monitoring (SHM) is using the guided waves. The major advantage of these waves is the low energy losing while passing through the structure, which denotes an excellent energy transfer through entire structure. The pioneer of this method is Horace Lamb which published his results for the first time in 1917 [24]. There exist two types of propagation modes for these waves: symmetric mode (S_0, S_1…S_n) and anti-symmetric (A_0, A_1…A_n) [25]. In many of the applications, the most used modes for SHM testing are the fundamental mode S_0, which is dominating at 150-300Hz and A_0 at 30-100Hz frequencies. The reason for choosing these two fundamental modes is that they are easier to identify from the oscillation group of modes than the other superior ones. The SHM testing technique was used to experimentally observe the first ply failure in the laminate plate.

The PWAS devices used in this experiment are produced by STEMiNCcompany, having the part number SMPL7W7T02412. They have a circular shape with 5 mm diameter and are presented in Fig. 9. The company code of the PWAS piezo-electric material is SM412 and the electro-mechanical properties are presented in the Table 5, [26].The input signal is a sinusoidal tone burst type signal having 20V peak to peak amplitude with Hanning window amplitude modulation. This signal includes 3 periods and it is generated by an Agilent 33120 signal generator, Fig. 10.

Fig. 9. PWAS positions on composite plate, geometry case 3

Table 5. Electro-mechanical characteristics of the SM412 material, [26]

Property	Symbol	Value	Measurement unit
Electromechanical coupling coefficient	K_p	0.63	
	K_t	0.42	
	K_{31}	0.35	
Frequency constant	N_p	2080	Hz ● m
	N_t	2080	
	N_{31}	1560	
Piezoelectric constant	d_{33}	450	$\times 10^{-12}$m/v
	d_{31}	-190	
	g_{33}	25.6	$\times 10^{-3}$Vm/N

	g_{31}	-12.6	
Elastic Constant	Y_{33}	5.6	$\times 10^{10} N/m^2$
	Y_{11}	7.6	
Mechanical Quality Factor	Q_m	100	
Dielectric Constant	$_{\varepsilon}T_{33/\varepsilon 0}$	1850	@1KHz
Dissipation Factor	tan δ	1.2	%@1KHz
Curie Temperature	T_c	320	°C
Density	r	7.8	g/cm^3

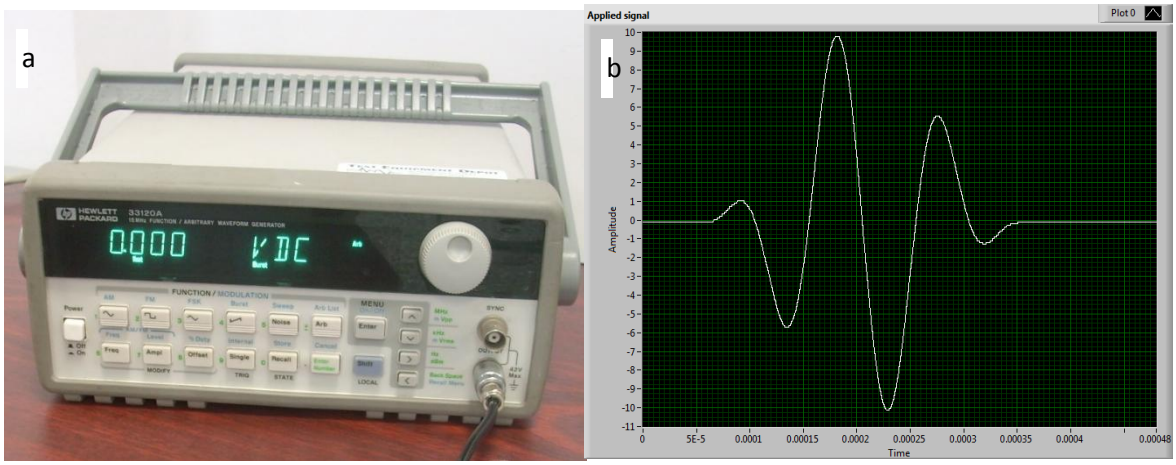

Fig.10. (a) Hewlett Packard 33120A arbitrary waveform generator, (b) input signal

This type of input signal provides a gradual excitation with progressive amplitudes of the joint structure.The received signal is registered by connecting an oscilloscope probe on receiving PWAS. For viewing the input signal also, an oscilloscope probe is connected to the emitting PWAS. This signal is used as reference signal for data processing. All these probes are connected to an Agilent DSO-X 3034A digital storage oscilloscope, Fig.11, which performs the data acquisition. The entire process of data acquisition, including the controll of the arbitrary wave form generator and the digital storage oscilloscope, is performed by a Labview code running on a PC. This PC is connected using USB and RS232C ports to the other devices as is shown in the Fig.12.

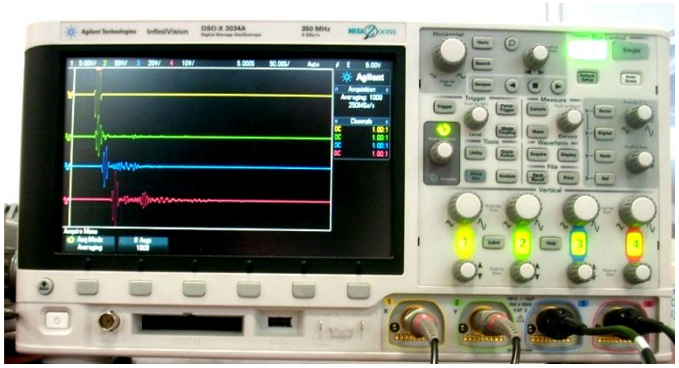
Fig.11. Agilent DSO-X 3034A digital storage oscilloscope

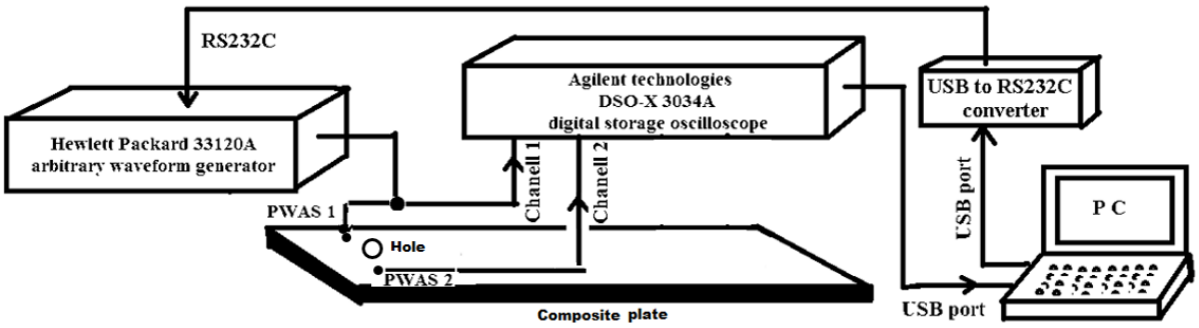

Fig.12. Block diagram of the acquisition system

In Fig. 13 it is presented the damage initiation effect on the amplitude of the received signal and force-displacement characteristic curve, in order to be able to identify the first ply failure of the laminated plate of the joint. The amplitude curve represent the maximum (peak to peak) amplitudes of each receiving signals during the test. During a test the input and output signals of the two PWAS's from the laminated plate are acquisitioned with a period of 2 seconds. From the Fig. 13 it can be clearly seen that the amplitude of output signal is increasing with the joint stiffening up to the first lamina failure event. Afterwards the amplitude is decreasing due to the elastic properties degradation in the laminate plate on the post failure stage. As a conclusion, it can be considered that SHM method accurately predict the first lamina failure and joint limit load which represents the fiber compression damage at the lamina level, because this local damage corresponds to a significant decreasing of the joint stiffness.

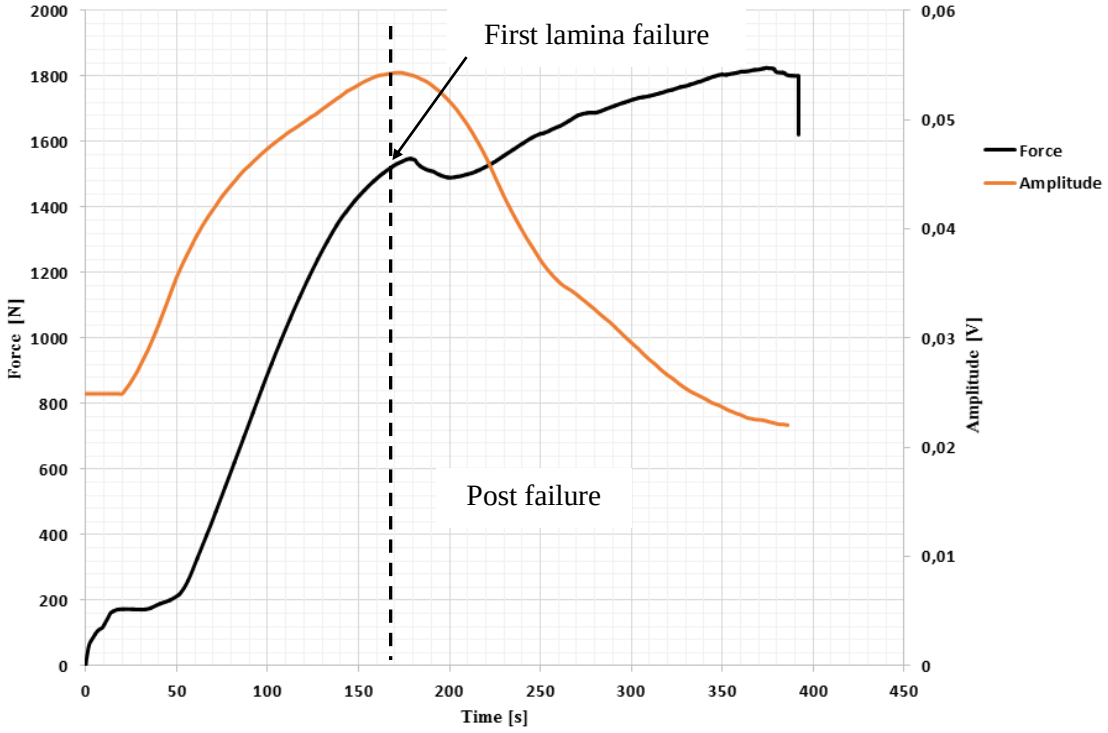

Fig. 13. Damage effects on output signal, geometry case 3

3.4 Nonlinear shear deformation

The simulation must take into account the two most important nonlinear mechanisms: lamina nonlinear shear deformations and stiffness reduction due to damage accumulation at lamina level. These two nonlinearities are taken into account using an external user-defined subroutine named USER_MAT, edited in FORTAN language. USER_MAT calls the modified Nastran material user-defined subroutine UMAT, in order to implement the material nonlinearities specified above. Hahn and Tsai developed [27] the in planenonlinear shear lamina constitutive model using high order elasticity theory:

$$\gamma_{12}=\frac{\tau_{12}}{G_{12}}+\beta\cdot\tau_{12}^{3}(1)$$

Where$\beta$is a material parameter that can be determined by experiments only.Fig. 14shows the experimental curve of the shear deformation γ_{12} as a function of the shear stress τ_{12} obtained using off-axis tension tests on unidirectional laminate.From the Fig. 14, by polynomial interpolation, it was obtained the coefficient β = 0.635 $(MPa)^{-3}$for this type of lamina used in the study.This constitutive relation can be implemented in USER_MAT user subroutine as it is described in [28]:

$$\tau_{12}^{(t+\Delta t)}=\frac{1+2\cdot\beta\cdot(\tau_{12}^{t})^{3}\cdot(\gamma_{12}^{t})^{-1}}{1+3\cdot\beta\cdot {G_{12}}^{0}\cdot(\tau_{12}^{(t)})^{2}}\cdot {G_{12}}^{0}\cdot\gamma_{12}^{t+\Delta t}(2)$$

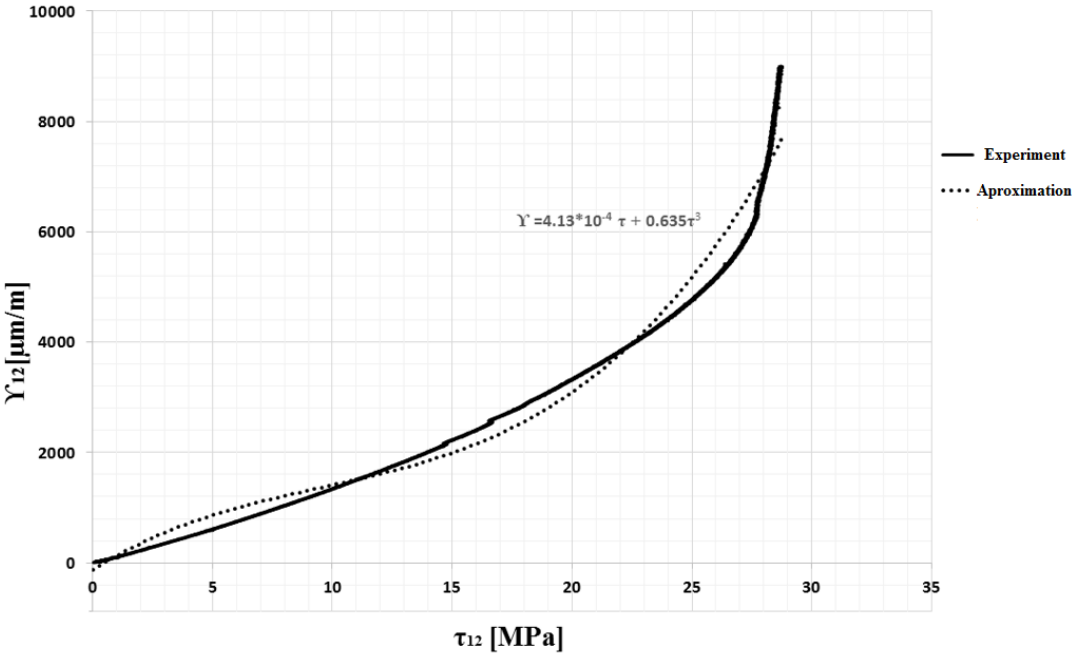

Fig. 14. Nonlinear shear–strain experimental curve

The orthotropic stress-strain constitutive relationship is given by equations (3) and (4), according to [28]:

$$\begin{bmatrix}\sigma_{11}^{t+\Delta t}\\ \sigma_{22}^{t+\Delta t}\\ \sigma_{33}^{t+\Delta t}\end{bmatrix}=\begin{bmatrix}E_{11}B(1-\vartheta_{23}\vartheta_{32}) & E_{22}B(\vartheta_{12}-\vartheta_{13}\vartheta_{32}) & E_{33}B(\vartheta_{13}-\vartheta_{12}\vartheta_{23})\\ E_{22}B(\vartheta_{12}-\vartheta_{13}\vartheta_{32}) & E_{22}B(1-\vartheta_{13}\vartheta_{31}) & E_{22}B(\vartheta_{32}-\vartheta_{12}\vartheta_{31})\\ E_{33}B(\vartheta_{13}-\vartheta_{12}\vartheta_{23}) & E_{22}B(\vartheta_{32}-\vartheta_{12}\vartheta_{31}) & E_{33}B(1-\vartheta_{12}\vartheta_{21})\end{bmatrix}\times\begin{bmatrix}\varepsilon_{11}^{t+\Delta t}\\ \varepsilon_{22}^{t+\Delta t}\\ \varepsilon_{33}^{t+\Delta t}\end{bmatrix}(3)$$

$$\begin{bmatrix}\tau_{12}^{t+\Delta t}\\ \tau_{23}^{t+\Delta t}\\ \tau_{31}^{t+\Delta t}\end{bmatrix}=\begin{bmatrix}Rel.(6) & 0 & 0\\ 0 & G_{23} & 0\\ 0 & 0 & G_{31}\end{bmatrix}\times\begin{bmatrix}\gamma_{12}^{t+\Delta t}\\ \gamma_{23}^{t+\Delta t}\\ \gamma_{31}^{t+\Delta t}\end{bmatrix}(4)$$

where:

$$B=\frac{1}{1-\vartheta_{12}\vartheta_{21}-\vartheta_{23}\vartheta_{32}-\vartheta_{13}\vartheta_{31}-2\cdot\vartheta_{21}\vartheta_{32}\vartheta_{13}}(5)$$

$$\tau_{12}^{t+\Delta t}=\begin{cases}\frac{1+2\cdot\beta\cdot(\tau_{12}^{t})^{3}\cdot(\gamma_{12}^{t})^{-1}}{1+3\cdot\beta\cdot {G_{12}}^{0}\cdot(\tau_{12}^{t})^{2}}\cdot {G_{12}}^{0}\cdot\gamma_{12}^{(t+\Delta t)}, & FI=0\\ {G_{12}}^{t+\Delta t}\cdot\gamma_{12}^{t+\Delta t}, & FI\geq 1\text{and}{G_{12}}^{t+\Delta t}\cdot\gamma_{12}^{t+\Delta t}<\tau_{12}^{init}\\ \tau_{12}^{init}, & FI\geq 1\text{and}{G_{12}}^{t+\Delta t}\cdot\gamma_{12}^{t+\Delta t}\geq\tau_{12}^{init}\end{cases}(6)$$

$$FI=max\ (FI_1, FI_2) \quad (7)$$

In relation (6), G_{12}^0 is the initial in-plane shear modulus which is reduced according to degradation rules specified in relation (11), once fiber compression-shear failure happened. The shear stress τ_{12}^{init} is a threshold used to avoid any over-estimation of the shear stress after any failure that can reduce the shear modulus G_{12}.

3.5 Failure criteria and continuous degradation rules

The most dominant micro-failure modes for bearing joints are matrix compression and fiber shear-compression failures, so an important attention is paid for them in this failure study. For the PDA of the laminated plate around the hole, Hashin [29] failure criteria is used and the failure indexes are calculated using relation (8) for matrix compression failure and relation (9) for fiber compression and matrix-fiber shear failure:

$$FI_1=\left[\left(\frac{\sigma^{C}_{22,\,max}}{2\cdot\tau^{max}_{23}}\right)^2-1\right]\cdot\frac{\sigma_2+\sigma_3}{\sigma^{C}_{22,\,max}}+\frac{(\sigma_2+\sigma_3)^2}{4\cdot(\tau^{max}_{23})^2}-\frac{\sigma_2\cdot\sigma_3}{(\tau^{max}_{23})^2}+\left(\frac{\tau_{12}}{\tau^{max}_{12}}\right)^2+\left(\frac{\tau_{13}}{\tau^{max}_{13}}\right)^2+\left(\frac{\tau_{23}}{\tau^{max}_{23}}\right)^2+\left(\frac{\sigma_1}{\sigma^{T}_{11,\,max}}\right)^2 \quad (8)$$

$$FI_2=\left(\frac{\sigma_1}{\sigma^{C}_{11,\,max}}\right)^2+\left(\frac{\tau_{12}}{\tau^{max}_{12}}\right)^2+\left(\frac{\tau_{13}}{\tau^{max}_{13}}\right)^2 \quad (9)$$

3.6 Continuous degradation rules for elastic moduli

A strain based degradation law is proposed for reduction of E_{ii} (i=1…3)as described in [30]. The fiber or matrix failure initiate at a user-defined failure strain ε_{ii}^{init} and PDA stiffness reductions are performed using [30]:

$$E_{ii}^{t+\Delta t}=\begin{cases}E_{ii}^0\cdot\left(1-d_i\cdot\dfrac{\varepsilon_{ii}^{t+\Delta t}-\varepsilon_{ii}^{init}}{\Delta\varepsilon_{ii}}\right), & \varepsilon_{ii}^{init}\le\varepsilon_{ii}^{t+\Delta t}<\varepsilon_{ii}^{init}+\Delta\varepsilon_{ii}\\ E_{ii}^0\cdot(1-d_i)\dfrac{\varepsilon_{ii}^{init}+\Delta\varepsilon_{ii}}{\varepsilon_{ii}^{t+\Delta t}}, & \varepsilon_{ii}^{t+\Delta t}\ge\varepsilon_{ii}^{init}+\Delta\varepsilon_{ii}\end{cases} \quad (10)$$

Where E_{ii}^0 is the initial modulus of elasticity from Table 2 for lamina orthotropic directions, $\Delta\varepsilon_{ii}$ is a user-defined strain step to ensure a smooth reduction of the properties upon failure and d_i is the reduction factor. Initial failure strain and corresponding stress ε_{ii}^{init}, σ_{ii}^{init} are determined by simulation for FI=1 according to relation (7).

3.7 Continuous degradation rules for shear moduli

The in-plane shear modulus G_{12} is continuous reduced using the maximum shear strain $\gamma_{ij}^{t+\Delta t}$ for FI>1, according to [30]:

$$G_{ij}=G_{ij}^0\left(0.1+0.9\cdot\frac{\gamma_{ij}^{init}}{\gamma_{ij}^{t+\Delta t}}\right),\ i\neq j=1\ldots3 \quad (11)$$

The reduction parameters for E_{ii}(i=1… 3) are presented in Table 6 and are obtained after several parameter tuning iterations.

Table 6.Degradation parameters for elastic moduli

Failure mode	d_i	$\Delta\varepsilon_{ii}$
Fiber shear-compression (i=1)	0.6	0.005
Matrix compression (i=2, 3)	0.8	0.005

3.8 Poisson's coefficient reduction

In [31] a continuous reduction of the Poisson's ratio is proposed in order to comply with elastic stability of the orthotropic materials:

$$\vartheta_{12}=\vartheta_{12}^0\cdot\sqrt{\frac{E_1E_2^0}{E_2E_1^0}},\ \vartheta_{13}=\vartheta_{13}^0\cdot\sqrt{\frac{E_1E_3^0}{E_3E_1^0}},\ \vartheta_{23}=\vartheta_{23}^0\cdot\sqrt{\frac{E_2E_3^0}{E_3E_2^0}} \quad (12)$$

3.9 Results and discussions

In order to better understand the nonlinear structural behavior and failure mechanisms in the joint, the load-displacement curves for the three geometric cases are presented in Fig. 15.

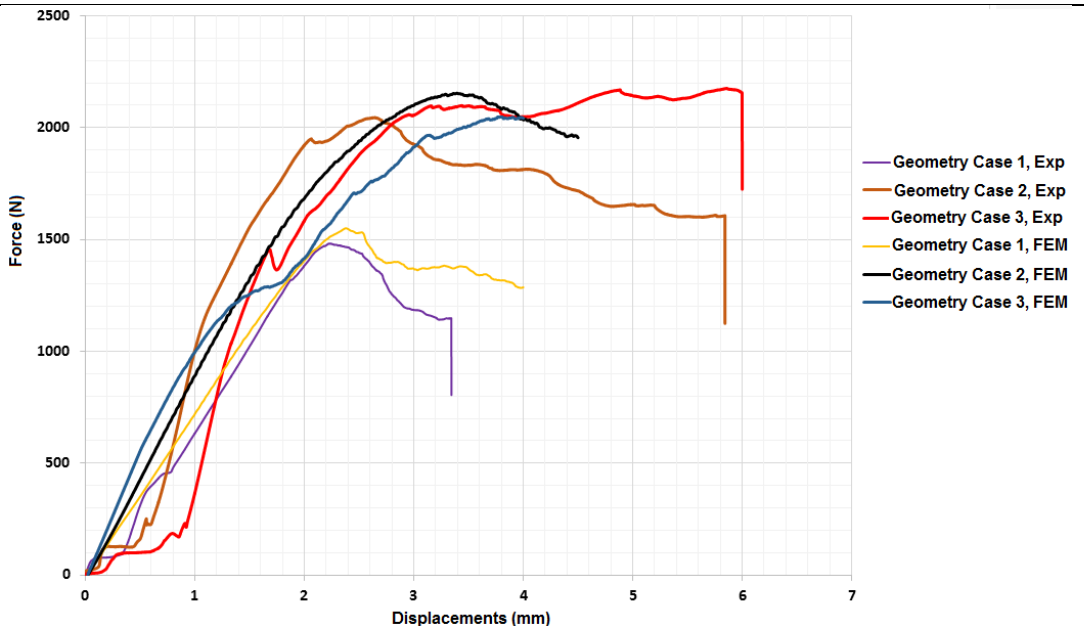

Fig. 15. Experimental and numerical load-displacement curves

The comparison between experimental and numerical results in terms of geometry effects on damage initiation and progressive failure mechanisms are presented in the following. Load-displacement curve for geometry case 1is presented in Fig. 16 and simulation results regarding progressive failure around the hole in the laminated plate are presented in Figs. 17-19. At the beginning of the experimental force-displacements curve it is observed a nonlinear behavior due to friction between the plates. Increasing the applied tensile load up to approximately 155 N, the plates will not move relative to each other, due to static friction between them and the applied loadis transmitted only by friction as discussed in joint stiffness subchapter. Point A represents the first damage initiation point, denoting the limit load of the joint and is located at the major deviation of the force-displacement curve from linear behavior. At this point, the fibers compression damage is firstly appeared as an indicator of the bearing failure initiation, despite the appearance of the fiber-matrix shear damage which is recorded in point A, also. Matrix compression damage is also present at point A, but this does not contribute to the joint stiffness loosening, because fibers have the most important role in joint stiffening, but not the matrix.

As can be seen from Fig. 17, in 0^o plies the fibers damage are more predominant than matrix damage, while in 90^o plies the two micro level damages have almost the same spread out. In Figs. 17-19, the dark blue color represents undamaged elements, while the red color states for E^0_{ii} $(1\text{-}d_i)$residual stiffness of the elements. From Fig. 17 it can be observed that the damaged layer is located to the top surface of the laminate, considering that the laminate plate was modeled with only one element per each ply in the thickness direction. The position of the first ply failure could be affected by the bolt tilting in the hole due to the exiting jointclearance and secondary bending effect.

In Fig. 16, point B represents the joint ultimate failure. After the point A, the damage accumulation determines joint stiffness reduction gradually and the characteristic curve becomes nonlinear. From point A up to B, the post failure stage is completely developed, where the residual stiffness is continuously reduced. On this stage, the fiber compression, matrix compression and fiber-matrix shear damages are increasing at the bearing plane through the whole thickness of the laminate plate, as can be seen from Fig. 18. Point C represents the catastrophic final failure of the joint, when fiber compression, matrix compression and fiber-matrix shear damages start and propagate on approximately +/- 45^odirections from loading axis and are extended to a large portion of the laminate plate on the bearing plane through free edge behind the hole of the plate, ascan easily be seen from Figs. 18 - 20.

Fig.16. Force-displacement curves. Geometry case 1

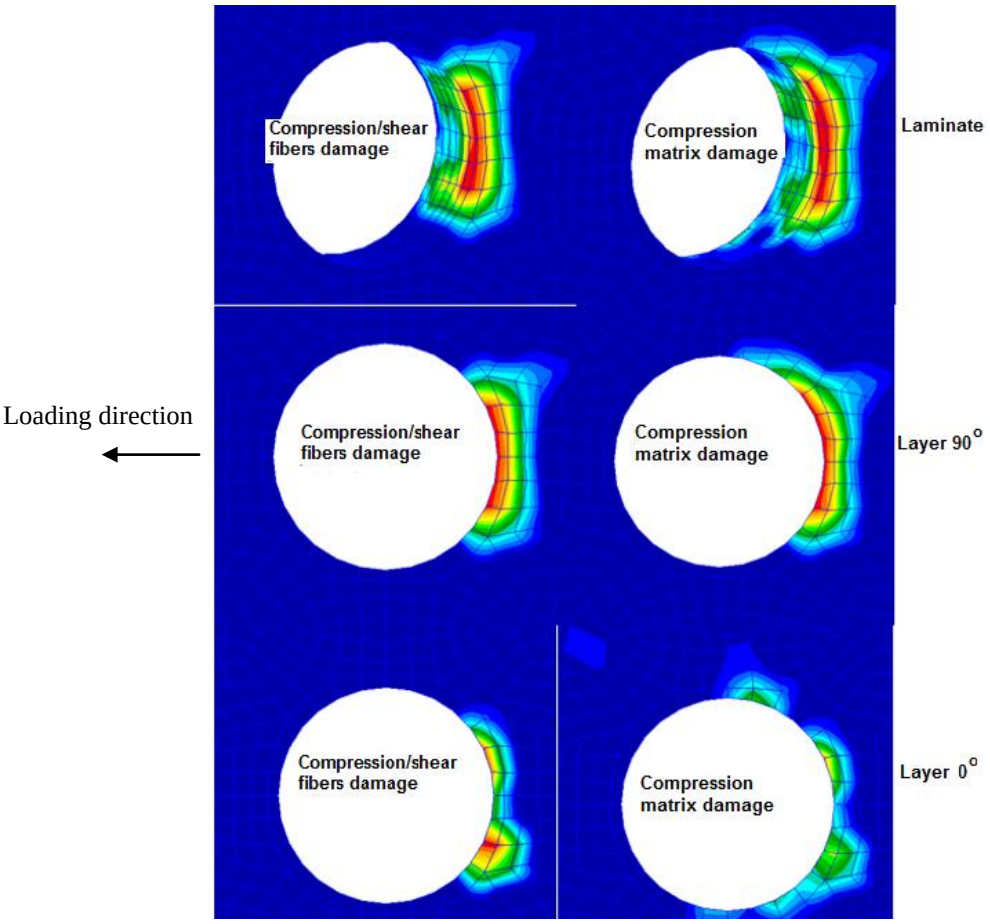

Fig. 17. Bearing damage initiation, point A.Geometry Case 1

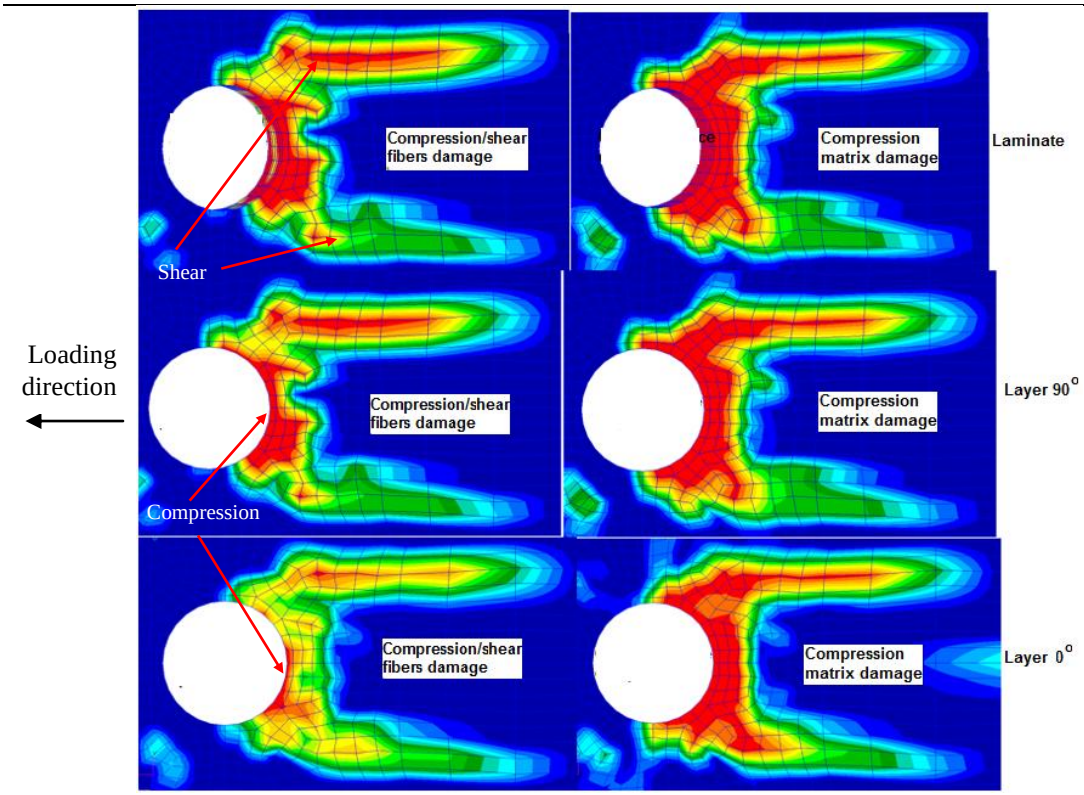

Fig. 18. Progressive damage, bearing/shear-out interaction, point B.Geometry case 1

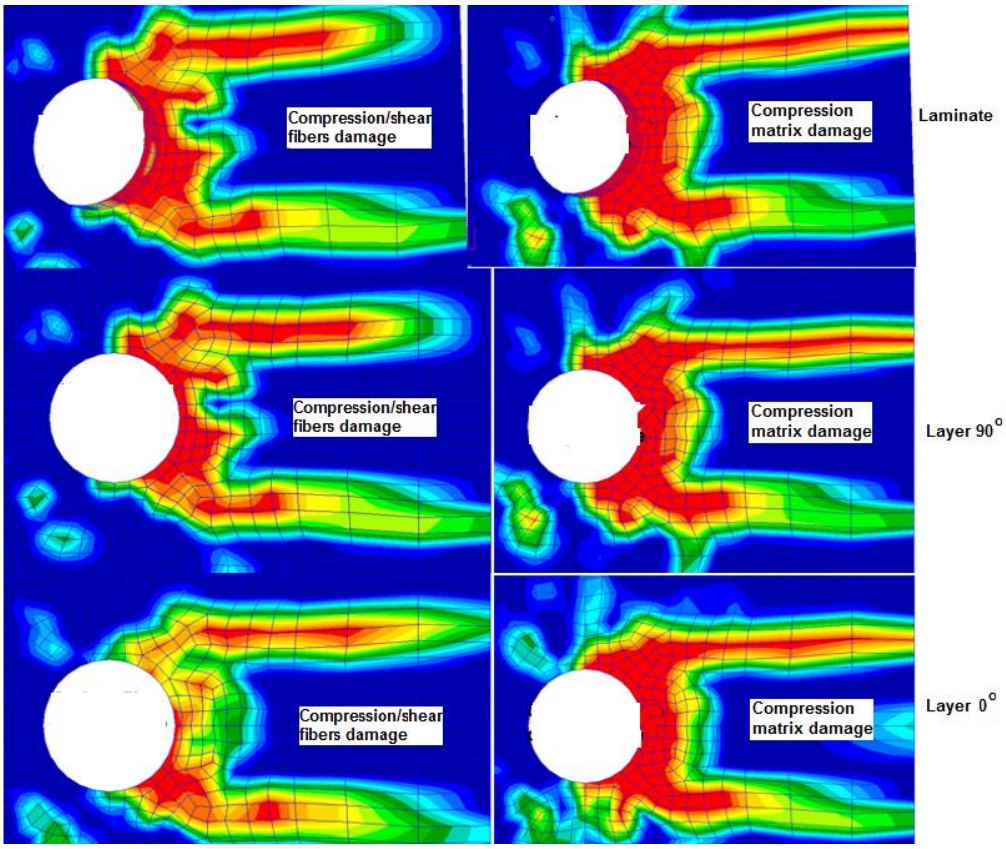

Fig. 19. Catastrophic failure, bearing/shear-out interaction, point C.Geometry case 1

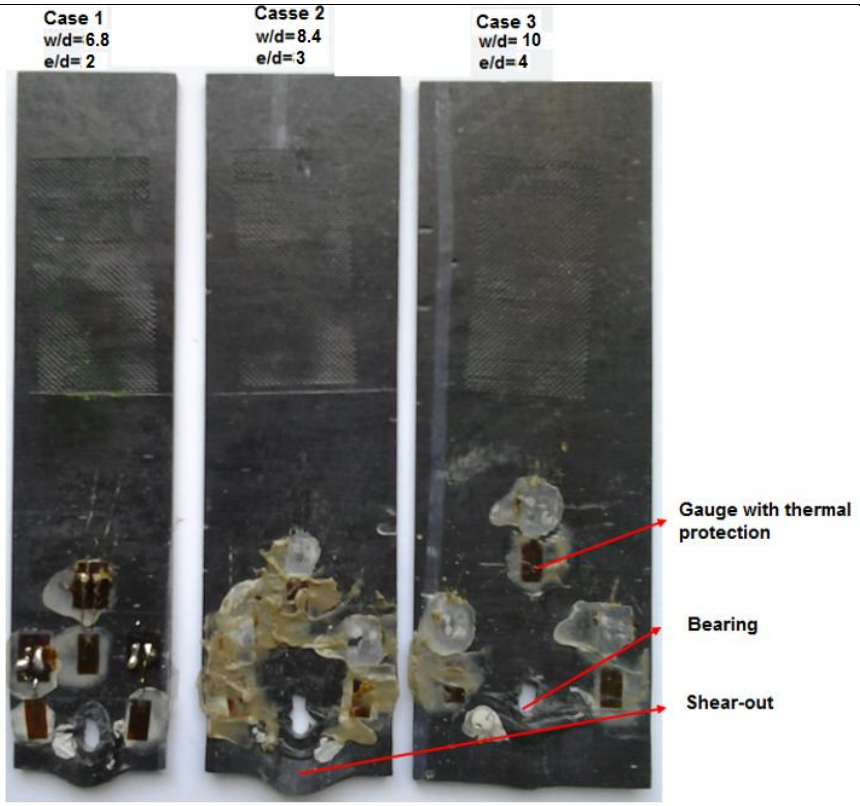

Fig. 20. The geometry influence on the joint failure modes

From Fig. 16, it can be observed that the friction static force between the aluminum and composite plates is approximately F_f= 150 N and taking into account the plates clamping force P = 330 N, implies that the real friction coefficient should be equal to:

$$\mu = \frac{F_f}{2 \cdot P} = \frac{150}{2 \cdot 330} = 0.22 \quad (13)$$

This value is quite closer to the values used in numerical simulation μ=0.235, according to Schon [23], which implies that the simulation took into account the friction base phenomena with sufficient accurate. The little difference between the friction coefficient values is due to the fact that in the experiments of this study the surfaces of the two plates were not properly cleaned with ultrasonic technique as Schon did in his work.

A summary of the geometry effects on the progressive failure of the metal-composite bolted joints is presented in Table 7 and Fig. 21. In Table 7,$F_{L.L.}$ and $F_{U.L.}$ represent the limit and ultimate loads of the joint to bearing failure and are corresponding to the A and B points from the characteristic force-displacements curves as discussed above. From the Table 7, it is clearly seen that bearing failure mode appears for all values of *w/d*, as the joint was designed in accordance with ASTM D 5961 standard [17] to induce bearing failure, but it is observed for values of *e/d*< 4, also. Shear-outfailure mode is present despite the fact that the literature research recommends *e/d*< 3 for this type of failure mode. In Fig.21 it is presented the influence of the geometric parameter *w/d*on the joint ultimate failure load and it can be seen that the curve has anasymptotic value of 2200 N for the ultimate failure load which denotes that for values *w/d*>10 are not recommended because have no more effects on the joint failure load.

Table 7. Geometry effects on macroscopic failure modes of the joints

Geometry case	T [^{o}C]	Torque [Nm]	$F_{L.L.}$ [N]		$F_{U.L.}$ [N]		Failure mode
			EXP	FEM	EXP	FEM	
w/d=6.8 *e/d* =2			1317.43	1376.65	1480.32	1548.94	Bearing/shear-out

w/d=8.4 *e/d*=3	50	0.5	1246.07	1225.65	2044.20	2043.94	Bearing/shear-out
w/d=10 *e/d*=4			1448.37	1500.03	2173.78	2151.84	Bearing

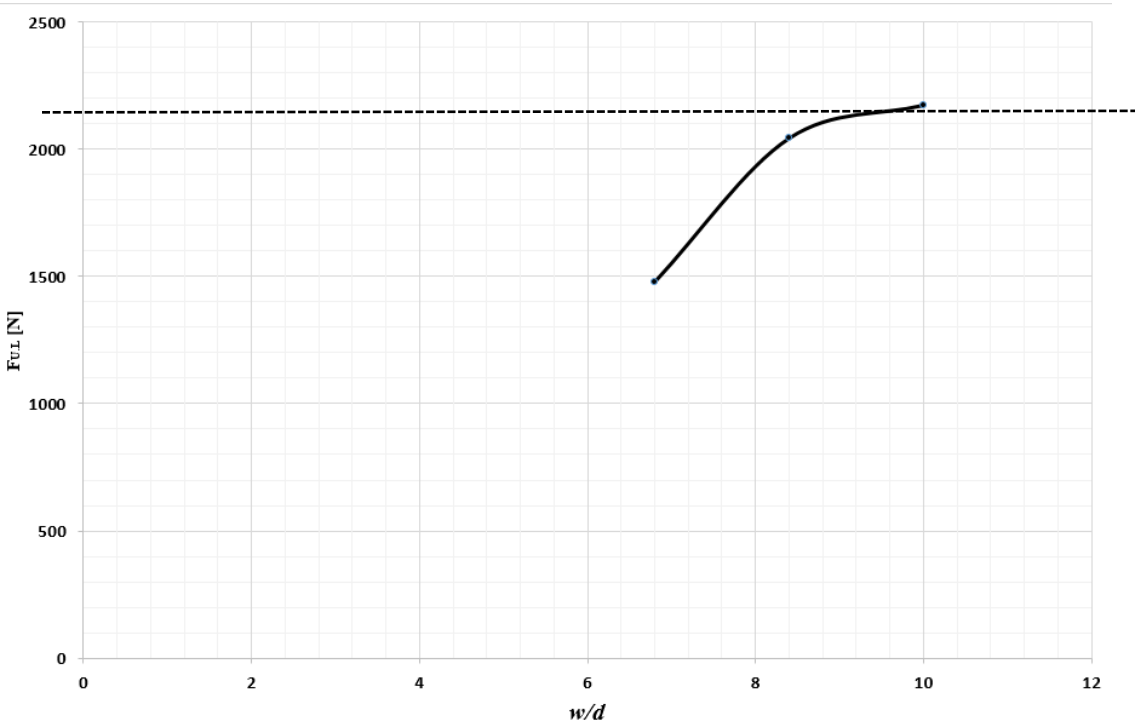

Fig.21.The influence of geometric parameter *w/d* on joint ultimate failure load

4. CONCLUSIONS

In this paper, the plate geometry effects on the damage initiation and progressive failure of single-lap, single-bolt, hybrid metal-composite joints are investigated using both SHM (Structural Health Monitoring) experimental nondestructive technique and numerical analysis with finite element method (FEM). Regarding the first ply failure (FPF) and strength evaluation, a progressive damage analysis (PDA) including lamina nonlinear shear behavior, Hashin failure criteria and strain-based continuous degradation laws was proposed. A 3D FEM model, which incorporates geometrical and contact full nonlinearities was developed in Patran as preprocessor and Nastran as explicit iterative solver. The PDA material model was implemented using a user-defined subroutine namely USER_MAT, using FOTRAN programming language.

The simulation results were in good agreement with the experiments in terms ofsurface strains, load-displacement response, FPF and ultimate failure loads, which denoted that the 3D FEM model including full nonlinearities and explicit solver algorithm are quite accurate and can predict the metal-composite joint's mechanical behavior on both linear-elastic and nonlinear ranges, including the failure modes as bearing and shear-out.Regarding the geometry effects on the load-displacement curves, it can be seen from the Fig.8 that the loading joint behavior released some interesting features at the beginning stage due to friction between the plates. This friction stage is composed from two parts: static and dynamic friction. From these graphs it can be detected the friction load and, knowing the clamping force from torque level, therefore the friction coefficient between the plates can be calculated. Regarding the FPF and strength predictions, the SHM technique proved to be quite accurate in evaluating the damage initiation and accumulation until final failure.

REFERENCES

[1] Y. Xiao, T. Ishikawa, Bearing strength and failure behavior of bolted composite joints (part II: modeling and simulation), *Composites Science and Technology,65(1),* 2005, 1032–1043.
[2] J.L.Chaboche,Continuum damage mechanics: part I – Generalconcepts; part II – damage growth, crack initiation and crackgrowth,*Journal of Applied Mechanics, 55,*1988, 59–72.
[3] F.K. Chang, K.Y. Chang, Post-failure analysis of bolted compositejoints in tension or shear-out mode failure,*Journal of Composite Materials,21,*1987,809–33.
[4] L.B. Lessard, M.M.Shokrieh, Two-dimensional modeling ofcomposite pinned-joint failure,*Journal of Composite Materials,29,*1995,671–97.
[5] C.L. Hung, F.K Chang, Bearing failure of bolted composite joints.Part II: model and verification,*Journal of Composite Materials,30,*1996,1359–400.
[6] S.J. Kim, J.S. Hwang, J.H. Kim, Progressive failure analysis of pin-loadedlaminated composites using penalty finite element method, *AIAA Journal,36(1),* 1998, 75–80.
[7] P.P.Camanho, F.L. Matthews, A progressive damage model formechanically fastened joints in composite laminates,*Journal of Composite Materials,33,* 1999, 2248–80.
[8] B.Okutan, The effects of geometric parameters on the failure strength for pin-loaded multi-directional fiber-glass reinforced epoxy laminate. *Composites B. Eng.33(8),* 2002, 567–8.
[9] K.I. Tserpes,G.Labeas, P.Papanikos, Th. Kermanidis, Strength prediction of bolted joints in graphite/epoxy composite laminates,*Compos. B. Eng. 33(7),* 2002, 521–9.
[10] Á.Olmedo, C.Santiuste, On the prediction of bolted single-lap composite joints,*Composite Structures, 94(6),*2012, 2110–7.
[11] Z.Kapidzˇic´, L.Nilsson, H. Ansell, Finite element modeling of mechanically fastened composite-aluminum joints in aircraft structures,*Composite Structures,109(6),*2014, 198–210.
[12] A.K.Zerbst, G.Kuhlmann, C.Steenbock, et *al*. Progressive damage analysis of composite bolted joints with liquid shim layers using constant and continuous degradation models,*Composite Structures, 92(2),*2010, 189–200.
[13] G.Kolks, K.I.Tserpes. Efficient progressive damage modeling of hybrid composite/titanium bolted joints,*Composites A,56(1),*2014, 51–63.
[14] B.Egan, M.A.McCarthy, R.M.Frizzell, P.J.Gray, C.T. McCarthy, Modelling bearing failure in countersunk composite joints under quasi-static loading using 3D explicit finite element analysis,*Composite Structures, 108,* 2014, 963–977.
[15] Á.Olmedo, C.Santiuste, E.Barbero, An analytical model for the secondary bending prediction in single-lap composite bolted-joints,*Composite Structures, 111,* 2014, 354–361.
[16] L.V.Awadhani, Dr. Anand K. Bewoor, Analytical and experimental investigation of effect of geometric parameters on the failure modes in a single lap single bolted metal to GFRP composite bolted joints subjected to axial tensile loading:*Proc. 4thICAAMM,* 2017, 7345–7350.
[17] *** ASTM D5961, *Standard test method for bearing response of polymer matrix composite laminates*, American Society for Testing and Materials, 2007.
[18] *** MMPDS-05, *Metallic Materials Properties development and Standardization*, Federal Aviation Administration, 2010
[19] ***ASTM D 3039, *Standard Test Method for Tensile Properties of Polymer Matrix Composite Materials*, ASTM International, 2007.
[20] *** ASTM D 5379, *Standard Test Method for Shear Propeties of Composite Materials by the V-Notched Beam Method*, ASTM International, 2008.
[21] *** ASTM D 3410, *Standard Test Method for Compressive Properties of Polymer Matrix Composite Materials*, ASTM International, 2007.
[22] M. A. McCarthy, C. T. McCarthy, V. P. Lawlor, W. F. Stanley, Three-dimensional finite element analysis of single-bolt, single-lap composite bolted joints: part I - model development and validation, *Composite Structures*, *71*, 2004, 140-158.
[23] Schon J. Coefficient of friction for aluminum in contact with a carbon fiber epoxy composite, *Tribology International,37(5),*2004, 395–404.
[24] H. Lamb, On Waves in an Elastic Plate, *Proc. of the Royal Society, Mathematical, Physical and Engineering Sciences*, *93*, 1917, 114 – 128.

[25] V.Giurgiutiu, J. Bao, Embedded Ultrasonic Structural Radar with Piezoelectric Wafer Active Sensors for the NDE of Thin-Wall Structures, *Proc. ASME International Mechanical Engineering Congress*, New Orleans, USA, 2002.

[26] *** http://www.steminc.com/piezo/PZ_property.asp.

[27] H.T.Hahn, S.W.Tsai, Nonlinear elastic behavior of unidirectional composite laminates,*Journal of Composite Materials, 7(1),*1973, 102–18.

[28] A. Du, Y. Liu, H. Xin, Y. Zuo, Progressive damage analysis of PFRP double-lap bolted joints usingexplicit finite element method,*Composite Structures, 152,* 2016, 860–869.

[29] Z.Hashin, Failure criteria for unidirectional fiber composites,*Journal of Applied Mechanics,80(47),* 1973, 329–342.

[30] Y. Zhou, H.Yazdani-Nezhad, M.A. Mccarthy, et *al*. A study of intra-laminar damage in double-lap, multi-bolt, composite joints with variable clearance using continuum damage mechanics,*Composite Structures,116 (9),* 2014, 441–52.

[31] RM. O'Higgins,*An experimental and numerical study of damage initiation and growth in high strength glass and carbon fibre-reinforced composite materials*, doctoral diss. University of Limerick, College of Engineering,Limerick, 2007.